

## RESEARCH ARTICLE

10.1002/2016JF003929

## Key Points:

- Meandering river centerline geometries encode process nonlinearities
- The net effect of cutoffs is to reduce overall form nonlinearity, but they also act as sources of nonlinearity
- Form nonlinearity depends not only on the size and shape of meander bends but also on their spatial arrangement

## Correspondence to:

J. Schwenk,  
jonschwenk@gmail.com

## Citation:

Schwenk, J., and E. Foufoula-Georgiou (2017), Are process nonlinearities encoded in meandering river planform morphology?, *J. Geophys. Res. Earth Surf.*, 122, 1534–1552, doi:10.1002/2016JF003929.

Received 20 APR 2016

Accepted 29 JUN 2017

Accepted article online 13 JUL 2017

Published online 9 AUG 2017

## Are process nonlinearities encoded in meandering river planform morphology?

Jon Schwenk<sup>1</sup>  and Efi Foufoula-Georgiou<sup>2</sup> 

<sup>1</sup>Earth and Environmental Sciences Division, Los Alamos National Laboratory, Los Alamos, New Mexico, USA, <sup>2</sup>Department of Civil and Environmental Engineering, University of California, Irvine, California, USA

**Abstract** Meandering river planform evolution is driven by the interaction of local nonlinear processes and cutoff dynamics. Despite the known nonlinear dynamics governing the evolution of meandering rivers, previous attempts have found at most a weak signature of these process nonlinearities within the meander planform morphologies (form nonlinearities). In this work, we present a framework to measure form nonlinearity from centerline curvature signals and unambiguously quantify its presence in both a numerically simulated meandering river and three natural rivers. The degree of nonlinearity (DNL) metric is introduced to measure the strength of form nonlinearities embedded in the centerlines. The DNL's evolution through time is computed for annual observations over 30 years of an active, tropical meandering river and for the simulated centerline to understand how cutoffs and bend growths affect form nonlinearity. We find that although cutoffs reduce the overall form nonlinearity, they also act as a source of nonlinearity themselves by creating scales that contribute disproportionately to DNL.

### 1. Introduction

The relationship between process and form is at the heart of many problems in geomorphology and holds particular intrigue in meandering rivers [e.g., Lane and Richards, 1997; Güneralp and Marston, 2012; Legleiter, 2014; Schwenk et al., 2015]. Meandering river planform morphology arises from the interaction of nonlinear local fluid and sediment dynamics along its course which typically act to grow, migrate, and/or deform bends. Cutoff dynamics also play an important role in shaping meander planform structure by immediately disconnecting meander bends and perturbing the local dynamics [Hooke, 2004; Camporeale et al., 2008; Schwenk and Foufoula-Georgiou, 2016]. The expression of formative meander dynamics through river morphology has received considerable attention via numerical experimentation wherein channel centerline characteristics such as sinuosity, wavelength, and average curvature depend on the implemented model dynamics [Sun et al., 2001; Camporeale et al., 2007; Motta et al., 2012; Schwenk et al., 2015]. On the other hand, empirical studies of meander morphodynamics approach the process-form link inversely by inferring meander dynamics from analyses of centerline structure under the assumption that the spatial structure somehow encodes properties of the governing dynamical system [Montgomery, 1993; Frascati and Lanzoni, 2010; Gutierrez and Abad, 2014; Zolezzi and Güneralp, 2015]. In this study, we investigate the validity of this assumption by determining whether nonlinearities known to be present in the deterministic dynamics of meander evolution are also expressed through the spatial centerline structure.

Physically based, reductionist theory of long-term meander evolution developed over the past four decades has identified *process nonlinearities* in the essential deterministic dynamics of meander evolution. We define process nonlinearities as those arising from process interactions (hydrodynamics, sediment dynamics, lateral migration, etc.) within a time-evolving, deterministic system and differentiate these from *form nonlinearities* which are expressed through the spatial structure of centerline morphologies formed by the evolving system. The existence of process nonlinearity was noted by Ikeda et al. [1981] who considered the equations of motion for treatment of finite-amplitude bends in intrinsic coordinates. This process nonlinearity of geometric origin (called herein a geometric process nonlinearity) is expressed through the development of higher-order modes of sine-generated curves [Parker et al., 1982; Seminara et al., 2001] by fattening and skewing meander bends. Seminara et al. [2001] later generalized this notion via geometrical arguments (their Figure 2) showing that any curve evolving through time is governed by

$$\frac{\partial \zeta}{\partial s} = \frac{\partial \theta}{\partial t} - \frac{\partial \theta}{\partial s} \int_0^s \zeta \frac{\partial \theta}{\partial s} ds, \quad (1)$$

where  $\zeta$  is the rate of lateral movement at some distance  $s$  along the curve,  $t$  is time, and  $\theta$  represents the angle of the curve with respect to the horizontal, and  $\partial\theta/\partial s$  is the curvature. This equation demonstrates a geometric process nonlinearity inherent in evolving meanders due to the quadratic form of  $\partial\theta/\partial s$  in the integral term evident from the evaluation of the integral at its upper limit. In addition to the geometric process nonlinearity of meander evolution, equation (1) may also include process nonlinearities arising from hydrodynamics, sediment dynamics, and/or their interaction expressed through the formulation of the lateral rate of migration ( $\zeta$ ). The earliest hydrodynamic models of flow through meander bends were achieved through perturbation analyses wherein the higher-order, nonlinear terms were discarded under the assumption of small centerline curvatures [e.g., Callander, 1969; Ikeda et al., 1981]. Eventually, 2-D depth-averaged nonlinear hydrodynamic models were developed that included the discarded nonlinear terms that capture the nonlinear coupling of downstream velocity with secondary cells that deform the vertical flow profile [Smith and McLean, 1984; Imran et al., 1999; Blanckaert and de Vriend, 2010]. The retention of these nonlinear terms in the governing hydrodynamic equations was shown to result in significantly different planform morphologies [Camporeale et al., 2007]. Although not yet applicable to the large spatial and temporal scales of meander migration considered here, three-dimensional, eddy-resolving models that explicitly capture rather than parameterize nonlinear physics have explicated further the complex and nonlinear hydrodynamics within meander bends [Keylock et al., 2012; Blanckaert et al., 2013; Constantinescu et al., 2014].

Nonlinearities associated with sediment dynamics have similarly been gradually included in models of meander evolution, though to a lesser extent than hydrodynamics. The nonlinear Exner equation accounting for conservation of mass is typically linearized [e.g., Seminara et al., 2001] and closed with (a) a nonlinear expression for bed load transport in the downstream direction; i.e.,  $q_{s,s} \sim (T - T_c)^m$  where  $T_c$  is critical bed shear stress, where  $q_{s,s}$  is sediment flux in the downstream direction,  $T$  is bed shear stress,  $T_c$  is critical bed shear stress, and  $m$  is a typically-non-unity exponent, and (b) an assumed transverse bed profile that is related either linearly [Johannesson and Parker, 1989], sinusoidally [Struikma et al., 1985], or exponentially [Blanckaert and de Vriend, 2010] to local curvature. The observation of longer time scales of bed adjustment relative to the time scales of hydrodynamic forcings (i.e., floods) is often used to justify decoupling the hydrodynamics and morphodynamics [Pittaluga and Seminara, 2011], but the resulting sediment dynamics may still be forced with a nonlinear flow field through  $\tau = f(\mathbf{u})$  for a velocity field  $\mathbf{u}$ . Of course, 3-D modeling using computational fluid dynamics (CFD) techniques includes the full coupling of the nonlinear hydrodynamics and morphodynamics and includes additional nonlinearities associated with turbulence [Rüther and Olsen, 2007; Kang and Sotiropoulos, 2012] and the expansion of the nonlinear terms of the Navier-Stokes and Exner equations into the third dimension. Computational costs prohibit CFD simulations of meander trains over long times, but fully characterizing the effects of deterministic nonlinearities on planform morphology would require no less.

In addition to the local deterministic nonlinear processes driving meander evolution, the cutoff process introduces a planform-scale threshold form nonlinearity through the sudden removal of bends. Cutoffs have been argued to reduce overall form nonlinearity by removing older bends that have had more time to express the deterministic nonlinear dynamics of meander evolution [Perucca et al., 2005; Seminara, 2006; Camporeale et al., 2008]. However, local dynamics see cutoffs as perturbations to the system's state variables (e.g., slope, sediment flux, and flow velocity) which may be magnified through the driving nonlinear dynamics and manifest through the planform morphology.

A handful of studies have suggested that meandering river planform morphodynamics exhibit chaotic behavior and self-organized criticality (SOC), both concepts requiring nonlinear system dynamics. Montgomery [1993] found evidence supporting a chaotic model for the curvature series of at least one natural river, although chaos was not similarly detected in simulated rivers [Frascati and Lanzoni, 2010]. The conceptualization of meandering rivers as SOC systems [Bak et al., 1987] was developed by Stolum [1997, 1998] and includes evidence from the power law size-frequency distribution of oxbow lakes created by a simulated river [Stolum, 1996] and avalanching cutoff dynamics along the Ucayali River [Schwenk and Foufoula-Georgiou, 2016]. Such phenomenological models require as a necessary condition a nonlinear dynamical system, but despite both theoretical justification for nonlinear processes driving planform evolution and empirical descriptions of planform morphodynamics by models requiring nonlinearity, direct attempts to detect and quantify form nonlinearity have been unsuccessful in both real [Perucca et al., 2005] and simulated [Frascati and Lanzoni, 2010] meandering centerlines. These studies cast signals of the spatial series of

curvature into a phase space in order to test their trajectories for nonlinear and/or deterministic structure and found at most weak evidence of nonlinearity, suggesting that process nonlinearities do not necessarily manifest as form nonlinearities in meandering river planform morphology.

In this work, we similarly investigate phase-space representations of curvature series but employ a less restrictive and more robust metric of nonlinearity. In section 2, we establish that the nonlinearities in the underlying meander evolution dynamics (process nonlinearities) are indeed manifest through the centerline curvature series of meandering rivers (form nonlinearity) in section 2. The effects of bend growth and cutoffs on form nonlinearity are investigated for evolving centerlines: first using a long-time simulation of a meandering river where the underlying deterministic dynamics are exactly known, and then for annual realizations of an actively migrating, tropical meandering river over 30 years (section 3). The sources of form nonlinearity are further interrogated by identifying scales that disproportionately contribute to nonlinearity using wavelet-based techniques (section 4). Implications of these results on the relationship between form and process in meandering rivers are discussed, as well as the caveats of interpretation (section 5), and future research directions are identified (section 6).

## 2. Is Form Nonlinearity Present in Natural Rivers?

The degree of nonlinear structure in a stationary signal, such as the curvature series of a river centerline, can be measured by comparing the signal with a surrogate of itself wherein its nonlinear structure has been destroyed, but its linear properties remain intact [Theiler *et al.*, 1992; Schreiber and Schmitz, 2000]. The signal and its surrogate are cast into a phase space where their (possibly) nonlinear structure is unfolded, and their difference is measured by the transportation distance (TD). Multiple surrogates may be generated of the same original signal to test whether a signal is significantly nonlinear and, if so, assess its degree of nonlinearity (DNL, Figure 1). In this section, the details of surrogate generation (section 2.1.1), embedding in a phase space (section 2.1.2), and computing the TD and DNL (section 2.1.3) are given, followed by the application of these techniques to two meandering rivers in Minnesota, USA (section 2.2).

### 2.1. Method for Detecting Nonlinearity

#### 2.1.1. Generating Completely Linearized Surrogates

Linear signals have statistical properties that are independent of their Fourier phases. For example, randomizing the Fourier phases of a signal has no effect on its autocorrelation structure yet destroys its nonlinear structure [Theiler *et al.*, 1992; Schreiber and Schmitz, 2000]. A signal is therefore considered nonlinear if the randomization of its Fourier phases results in a significantly “different” signal [Kantz and Schreiber, 2004]. Such modified signals, called surrogates, were introduced by Theiler *et al.* [1992] and have since been widely applied [see Schreiber and Schmitz, 2000].

A modified iterated amplitude adjusted Fourier transform (IAAFT) was used to generate a linear surrogate  $\hat{C}(s)$  from a spatial series of curvatures  $C(s)$  in four steps [see Keylock, 2007, 2008]. Our procedure for computing curvature series from centerlines is laid out in Appendix A. First, the Fourier transform decomposed the signal  $C(s)$  into a series of various-frequency sinusoids, each with an associated amplitude and phase. Second, the phases of the component sinusoids were randomized, but the amplitudes were preserved. Third, the inverse Fourier transform returns a signal  $\hat{C}(s)$  with the same power spectrum. Finally, the values of  $\hat{C}(s)$  are replaced by those in  $C(s)$  via a rank-order matching process in order to ensure the same distribution of the original and surrogate series. This final step may cause minor mismatching between the original and surrogate spectra, and thus, the entire procedure is iterated until a convergence criterion is met [Schreiber and Schmitz, 1996; Venema *et al.*, 2006]. The surrogate ultimately has the same values (probability distribution) and Fourier spectrum (autocorrelation) as the original signal. Multiple surrogates may be generated from the same original signal by performing different phase randomizations.

#### 2.1.2. Casting Signals and Surrogates Into Embedding Space

When a system's evolution equations are known a priori, it can be projected into a phase space whose axes are the independent variables of the system, and the system's evolution through time is represented by a trajectory through the phase space. In many systems, including meandering rivers, the complete set of evolution equations are unknown, but time or space series of one or more system variables are available. In these cases, Takens theorem [Takens, 1981] provides a method of reconstructing a trajectory of the dynamic

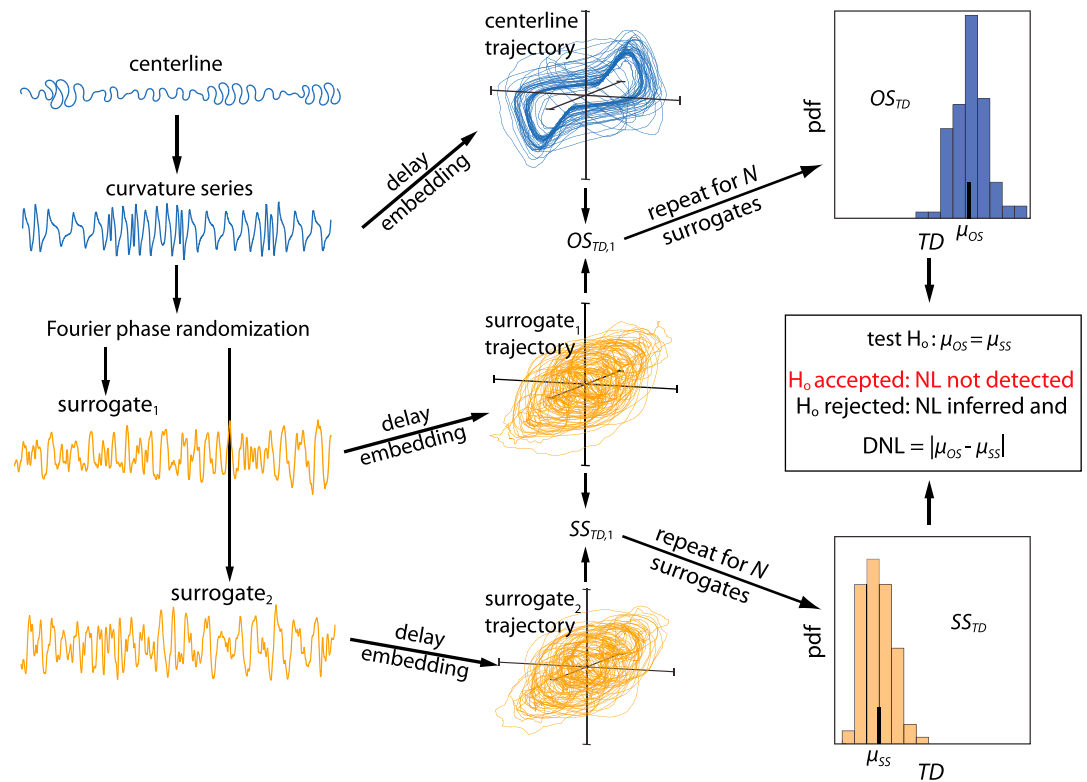


**Figure 1.** The procedure for testing centerlines for nonlinearity and computing the degree of nonlinearity (DNL) is shown. First, the curvature series is computed (see Appendix A).  $N$  surrogates of the curvature series are generated (only two are shown) by randomizing their Fourier phases. The curvature series and its surrogate are embedded in phase space and the difference between original-surrogate trajectories ( $OS_{TD,1}$ ) is measured by the transportation distance (TD). This procedure is repeated  $N$  times, resulting in the  $OS_{TD}$  distribution. The same procedure is used to generate the  $SS_{TD}$  distribution except that surrogate-surrogate pairs are compared in the embedding space. A  $t$  test is performed to test the hypothesis ( $H_0$ ) that the mean of  $OS_{TD}$  ( $\mu_{OS}$ ) and  $SS_{TD}$  ( $\mu_{SS}$ ) are drawn from the normal distributions with equivalent means at a 99% confidence level. If  $H_0$  is rejected, nonlinearity (NL) is inferred and the DNL is computed as the absolute difference between  $\mu_{OS}$  and  $\mu_{SS}$ .

system from a single measurement (i.e., a time or space series) on the system via a technique termed *delay embedding*, provided that the measurement is fully coupled to the system dynamics.

We assume the spatial series of curvatures as a measurement coupled to the complete dynamic system and construct an  $m$ -dimensional embedding space with delay vectors of the curvature series:

$$\vec{C}_m = (C_{n-(m-1)\tau}, C_{n-(m-2)\tau}, \dots, C_n), \quad (2)$$

where  $m$  is the dimension of the embedding space and  $\tau$  is the lag. For a given series of length  $n$ , a total of  $n-(m-1)\tau$  points will be contained in each of the  $m$  vectors. The embedding dimension  $m$  should roughly correspond to the number of independent variables in the dynamic system. Selection of  $m$  was guided by an evaluation of “false nearest neighbors,” which are points in phase space that are nearby in lower dimensions but separate when cast into a higher-dimensional phase space [Abarbanel and Kennel, 1993]. In practice, the selection of  $m$  is constrained by the length of the signal, and large  $m$  vectors are computationally infeasible. We tested  $m = 2, 3, 4$  and found the results insensitive in agreement with others [e.g., Moeckel and Murray, 1997; Basu and Fofoula-Georgiou, 2002] and thus used  $m = 3$  for all analyses herein. The lag  $\tau$  should be large enough to remove significant linear correlation between subsequent points in  $\vec{C}_m$ , which we estimated as the lag of the zero crossing of the series’ autocorrelation function.

We note that delay embedding to reconstruct system trajectories is typically performed using a dynamic measurement on the system, i.e., a variable changing in time [e.g., Hegger et al., 1999], although spatial embedding has been performed as well [e.g., Keylock et al., 2014]. The degree to which processes may be

inferred from form depends entirely on the validity of the assumption that the spatial series of curvatures is a sufficient measurement on the dynamical system governing meander evolution. This assumption is physically justifiable, in that a centerline curvature series integrates dynamics of local processes driving channel migration, cutoffs, and the feedbacks between them, but it also requires that established process nonlinearities (i.e., those discussed in section 1) must be detectable in the phase space representations. The following section describes our method for detecting nonlinearity of signals cast into a phase space.

### 2.1.3. Computing Transportation Distance and Degree of Nonlinearity

The trajectories of each original curvature series and its linearized counterpart were reconstructed in phase space via delay embedding, and the difference between the signals was estimated as the “distance” between the density distribution of the two trajectory geometries within the embedding space. This measure was developed by Moeckel and Murray [1997] as the transportation distance (TD) and is equivalent to the more intuitive Earth mover’s distance [Rubner et al., 2000] which simply measures the minimum amount of work required to transform one pile of dirt into another pile, where work is the amount of dirt to be moved times the shortest distance it must be moved [Kantorovich, 1942; Ning et al., 2015]. In our case, the piles of dirt are the densities of each trajectory within the embedding space, and the minimum amount of work required is the TD [Moeckel and Murray, 1997]. The details of computing the TD are given in Appendix B. Larger TD indicates a greater difference between the structure of the two trajectories and implies a greater dissimilarity between their underlying dynamic systems. Because distances are measured in an embedding space whose axes are defined by lagged vectors of the original signals, TD has units of the input signals. Other nonlinear metrics (e.g., Lyapunov exponents) are notoriously difficult to measure in real systems due to noise and insufficient signal length, but the TD has been shown to be more robust and revealing [Basu and Foufoula-Georgiou, 2002].

Next, we test statistically whether the original signal is significantly different from its linearized surrogates. The uncertainty of TD was estimated by generating  $N$  surrogates for each original signal. The TD was measured between each original-surrogate pair (OS) and  $N$  surrogate-surrogate pairs (SS), resulting in two distributions of TD:  $OS_{TD}$  and  $SS_{TD}$ . Given  $N$  surrogates, there are  $N(N-1)/2$  possible unique surrogate-surrogate pairs. Of these,  $N$  surrogate-surrogate pairs were randomly selected by ensuring that each surrogate was compared exactly twice and never against itself. We adopted a  $t$  test statistic to test the null hypothesis that  $\mu_{OS}$  and  $\mu_{SS}$ , where  $\mu_{OS}$  ( $\mu_{SS}$ ) denotes the mean of the OS (SS) distribution, are drawn from normal distributions with the same mean at a 99% confidence level. If the null hypothesis were rejected, the signal was considered to be nonlinear. A demonstration of the ability of the TD to discriminate between linear and nonlinear signals is given in Appendix B. If a signal is found to be nonlinear, its degree of nonlinearity (DNL) may be measured as

$$DNL = |\mu_{OS} - \mu_{SS}|. \quad (3)$$

The DNL provides a measure of the degree of difference in the nonlinear structure of a signal and its linear counterpart. Confidence intervals were computed for each DNL according to

$$CI_L^U = DNL \pm z_{.99} \left( \frac{\sigma_{OS}}{\sqrt{N}} + \frac{\sigma_{SS}}{\sqrt{N}} \right), \quad (4)$$

where  $CI^U$  is the upper confidence bound,  $\sigma_{OS}$  is the standard deviation of the  $OS_{TD}$  distribution, and  $z_{.99}$  refers to the number of standard deviations extending from the mean of a normal distribution to account for 99% of its probability of nonexceedance.

## 2.2. Nonlinearity in Two Meandering Rivers

The single-threaded, meandering Blue Earth and Watonwan Rivers in Minnesota, USA, were mapped at two times from aerial photography taken in 1938 and 2008 (Figure 2). The Watonwan is a tributary to the Blue Earth, and both rivers flow through a watershed dominated by row crop agriculture (80% coverage). The hydrologic regime shifted substantially around the 1970s due to a combination of anthropogenic and climate changes [Foufoula-Georgiou et al., 2015]. Migration rates along both rivers were highly spatially variable between 1938 and 2008, but the Blue Earth migrated an average of 0.26 m/yr compared with the Watonwan’s 0.15 m/yr. Over the 70 year period, the Blue Earth underwent 22 cutoffs but grew 1.1 km

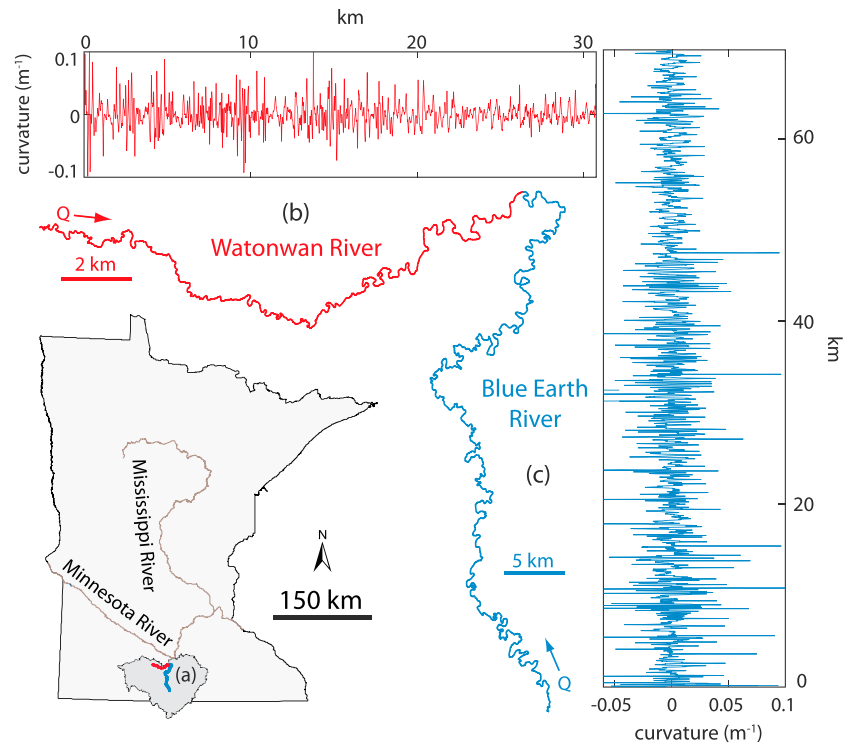


**Figure 2.** The locations of the Blue Earth (in red) and Watonwan (in blue) rivers are shown within the Greater Blue Earth Basin (a) in Minnesota, USA. (c and d) The 2008 Watonwan River and 2008 Blue Earth centerlines are shown in more detail along with their curvature series. As shown, both rivers flow to the same location but note the different scales for each.

longer, while 14 cutoffs occurred along the Watonwan, and its length was reduced by 2.0 km. The Watonwan widened by 19%, and the Blue Earth by 11% over the same period. Planform and migration characteristics for both rivers are given in Table 1.

The centerlines of the Blue Earth and Watonwan Rivers in both 1938 and 2008 exhibited significant form nonlinearity, evident from the nonoverlapping  $OS_{TD}$  and  $SS_{TD}$  distributions in Figure 3. For both rivers, the degrees of nonlinearity (DNLs) decreased over the 70 year period: 4.0% for Watonwan and 12% for Blue Earth. The larger reduction of DNL in the Blue Earth River may reflect the 22 cutoffs that occurred between 1938 and 2008, compared with the Watonwan’s 14. Migrated area maps show that the planform morphology of both rivers changed significantly, but the reaches’ sinuosities changed only 3% and 0.6% for the Watonwan and Blue Earth, respectively.

### 3. The Evolution of Nonlinearity

A meandering river’s degree of nonlinearity depends on the evolution of its bends and their removal through cutoff. Understanding the relative importance of bend evolution and removal to the overall

**Table 1.** Characteristics of the Analyzed Minnesota Rivers

River	Width (m)		Length (km)		Sinuosity		Slope	$M_r^a$		$A_{cutoff}/A_{river}^b$
	1938	2008	1938	2008	1938	2008		m/yr	Cutoffs	
Watonwan	24.5	29.1	61.3	59.3	2.28	2.21	$5.2 \times 10^{-4}$	0.15	14	15.8
Blue Earth	45.4	50.4	165.5	166.6	2.94	2.96	$5.2 \times 10^{-4}$	0.26	22	8.9

<sup>a</sup>Migration rate ( $M_r$ ) is computed as  $A_{mig}/length/1$  year, where  $A_{mig}$  is the area the centerline traversed between two realizations in time.

<sup>b</sup> $A_{cutoff}$  is the area encompassed by a cut off portion of centerline, and  $A_{river}$  is the planform area of the channel.

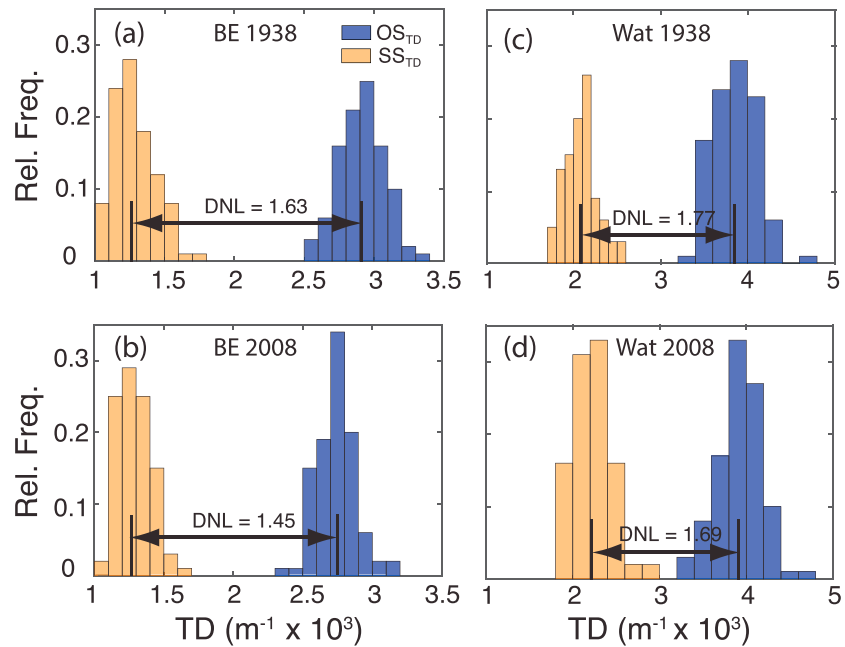


**Figure 3.** The distributions of transportation distances (TDs) between the original centerline curvature series and their surrogates ( $OS_{TD}$ ) and between surrogates and surrogates ( $SS_{TD}$ ) are shown for the Blue Earth River, (a) 1938 and (b) 2008 and the Watonwan River, (c) 1938 and (d) 2008. The degree of nonlinearity (DNL) is shown as the distance between the means (vertical black lines) of the  $OS_{TD}$  and  $SS_{TD}$  distributions. Units of DNL are the same as TD ( $m^{-1} \times 10^3$ ).

DNL requires observations with sufficient temporal resolution to capture these effects. To this end, we analyze the time evolution of the centerline DNL from a simple numerical long-time model of meander migration (section 3.1). Additionally, annual observations of the dynamic, meandering Ucayali River over a 30 year period give insight into the relationship between centerline growth, cutoffs, and DNL in a natural setting (section 3.2).

### 3.1. Evolving Nonlinearity in a Simulated Planform

We used a simple, long-time numerical simulation of a constant-width, migrating, meandering channel with a linearized solution for the flow field and a linear migration rule [Ikeda *et al.*, 1981]. Sediment dynamics are decoupled from hydrodynamics, and the transverse bed profile is computed as a linear function of the local curvature. The curvature-driven model, including parameters and boundary conditions, is described in detail and offered as downloadable MATLAB scripts in Schwenk *et al.* [2015]. The centerline is initially straight with small Gaussian perturbations that evolve into somewhat uniform bends until cutoffs begin. Cutoffs introduce discontinuities in the centerline which are expressed as high-frequency (small wavelength) perturbations in curvature that drive initial rapid bend migration and growth. Over time the planform dynamics through the occurrence of cutoffs give rise to a rich assortment of bend morphologies and lower frequency centerline excursions. That is, as the model progresses from the initially straight centerline, the channel develops large-scale features due to its lateral wandering throughout the domain. The linearization of the hydrodynamics and sediment dynamics and decoupling of the fluid and sediment interactions implies that any observed form nonlinearities must arise from process nonlinearities which are either geometric in nature (i.e., equation (1)) or due to cutoff dynamics.

We measured the DNL of the evolving curvature signal from the initially straight centerline for 39,000 years of simulated meander evolution (Figure 4). The centerline was initially 56 km and eventually fluctuated around a mean value of 190 km, although low-frequency periodicities are present due to the development of meander trains in the cross-valley direction. A slight tendency for centerline length to grow through time (1 km/20,000 years) results from a freely migrating downstream centerline node. Figure 4b shows that in the precutoff state, DNL grew nearly monotonically as the planform developed meander trains populated by individual

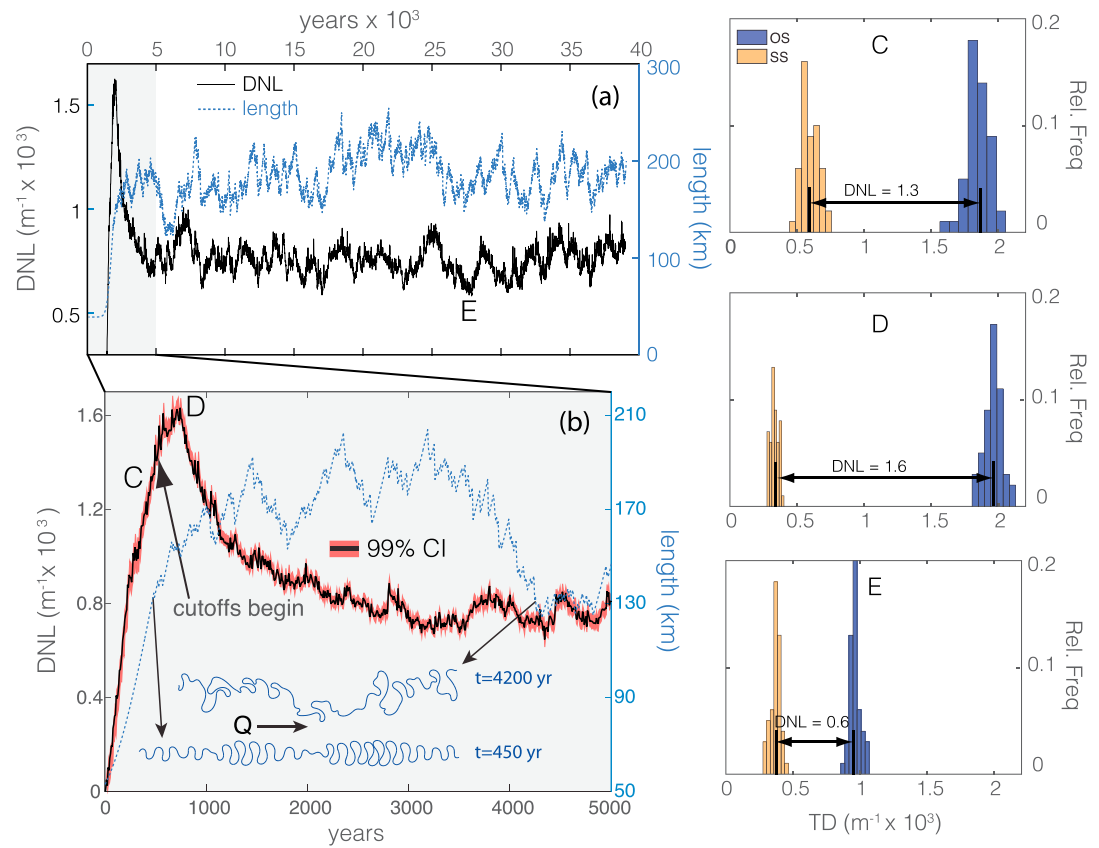


**Figure 4.** (a) The evolution of the degree of nonlinearity (solid black line) is shown for 39,000 years of the simulated centerline, and the centerline length is shown as a dotted blue line. (b) A closer view of the initial evolution and the transitional period is shown. The 99% confidence bounds for DNL are shown in orange. An arrow denotes the year (480) when cutoffs began. A precutoff centerline from year 450 and postcutoff centerline from year 4000 are shown. Flow is from left to right. (c–e) The  $OS_{TD}$  and  $SS_{TD}$  distributions are shown to verify that significant nonlinearity is present in precutoff, transitional, and postcutoff conditions. Figure 4c marks a precutoff centerline, Figure 4d represents the maximum DNL, and Figure 4e shows a local minimum of the DNL. DNL has the same units as TD ( $m^{-1} \times 10^3$ ).

bends that became larger and more asymmetric. After cutoffs began occurring, the DNL continued to increase for a short period of 250 years before attaining a maximum value. During this period, the effect of cutoffs to reduce the DNL was weaker than the contributions of bend growth to bolster the DNL. Both length and DNL also exhibited sustained increases and decreases of approximately 2–5000 years throughout the simulation (Figure 4a). Generally, periods of longer centerlines corresponded to periods of larger DNL, but the occurrence of individual cutoffs did not necessarily result in an immediate reduction in the DNL.

### 3.2. Evolving Nonlinearity of the Ucayali River

The Ucayali River in Peru is a highly active, sand-bedded, predominantly meandering channel originating in the Andes Mountains and flowing through the Amazon before joining the Amazon River. Using Landsat imagery, annual realizations of Ucayali centerlines were obtained from 1984 to 2015 (see Schwenk *et al.* [2016] for processing methods). Over this 30 year period, the 700 km study reach of the Ucayali (Figure 5) underwent 42 cutoffs while migrating an average of 51 m/yr. With an average bankfull width of 825 m, the Ucayali’s width-normalized migration rate is an order of magnitude larger than the Minnesota rivers’, permitting a faster planform response to flow and sediment pulses and perturbations due to cutoff. The Ucayali widened by 20% between 1985 and 2015.

The Ucayali River underwent significant planform change in the observed 30 year period (Figure 5). In particular, in 1997 a major 73 km triple-lobed cutoff near Masisea set off an avalanche of smaller

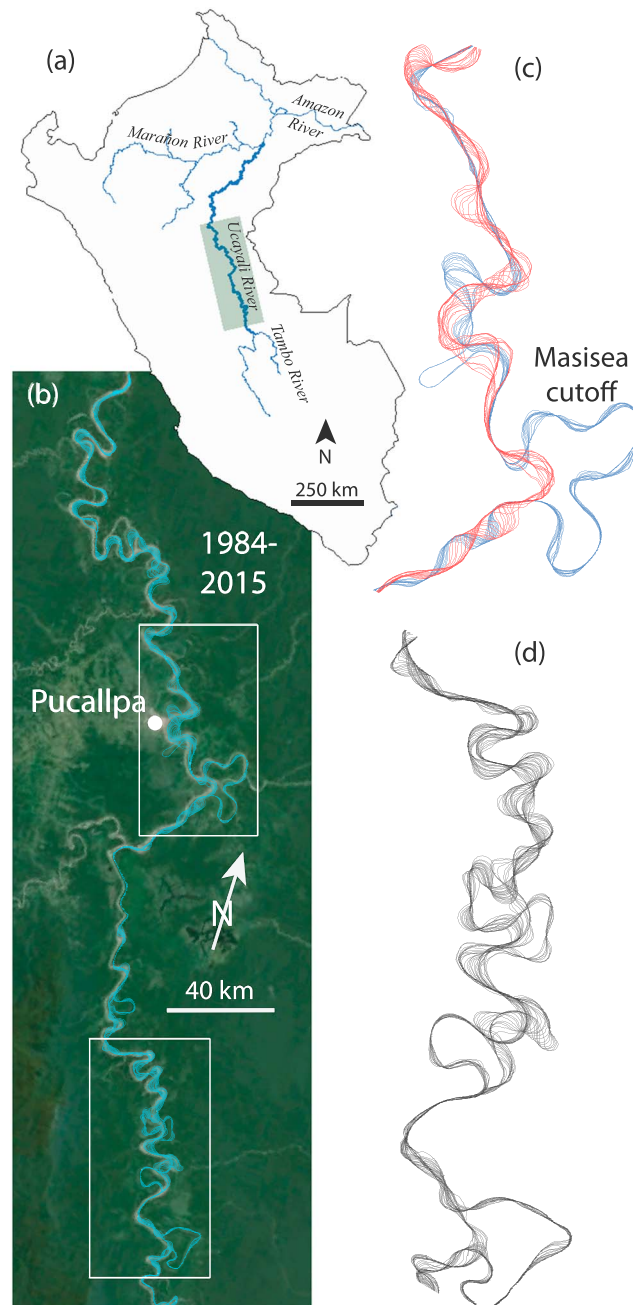


**Figure 5.** The reach of the Ucayali River, Peru, analyzed in this study is shown. (a) Map of Peru showing the analyzed reach of the Ucayali. (b) A zoom view of the green box, where annual centerlines from 1984 to 2015 are plotted atop aerial imagery from 2013. Details of centerline extraction are given in *Schwenk et al.* [2016]. (c) The effects of the 1997 cutoff of the triple lobed, 73 km bend on channel morphodynamics, are shown at a closer view. Pre-Masisea cutoff centerlines are blue; postcutoff red. (d) Planform centerlines for an active southern portion of the reach are shown in more detail. Aerial imagery is from Google Earth.

cutoffs, accelerated migration rates, and channel elongation both upstream and downstream of the Masisea cutoff [*Schwenk and Foufoula-Georgiou*, 2016]. From 1985 until the occurrence of the 1997 Masisea cutoff, the DNL of the Ucayali River grew in conjunction with net centerline growth over the period (Figures 6a and 6b). The Masisea cutoff resulted in the largest net shortening of the reach over the 30 year period and corresponded to the largest single-year decrease of the DNL over the same period. From 1997 to 2006, the Ucayali River underwent a series of cutoffs resulting in a net shortening of its centerline. This period corresponded to a reduction in the DNL as well, until it attained its minimum value in 2006. From 2006 to 2015, the Ucayali centerline experienced net growth, and the DNL again rose during this period. These observations agree with those of the simulation in that cutoffs tend to decrease the DNL, but a single cutoff event may not result in a lower DNL. For example, in 2002 the second-largest net reduction in channel length occurred, but the DNL increased slightly. Conversely, bend growth enhanced the DNL, as observed in Figure 6 where periods of reach lengthening generally correspond to periods of increasing DNL. However, this relationship does not hold across all years; for example, in 2004 the reach shortened by 17 km but the DNL nearly doubled. The DNL only slightly responded to the Masisea cutoff event itself but changed more drastically as subsequent accelerated bend growth and cutoffs occurred, apparently somewhat independently of their size. It is interesting to note that while the DNL eventually returned to pre-Masisea cutoff magnitudes (by 2014), the reach length remains 11% shorter than pre-Masisea cutoff and is “recovering” at a much slower pace than DNL.

These results suggest that DNL is not strictly related to the magnitude of bend removal through cutoff or elongation due to bend growth. Because DNL measures the complete centerline structure, the location of

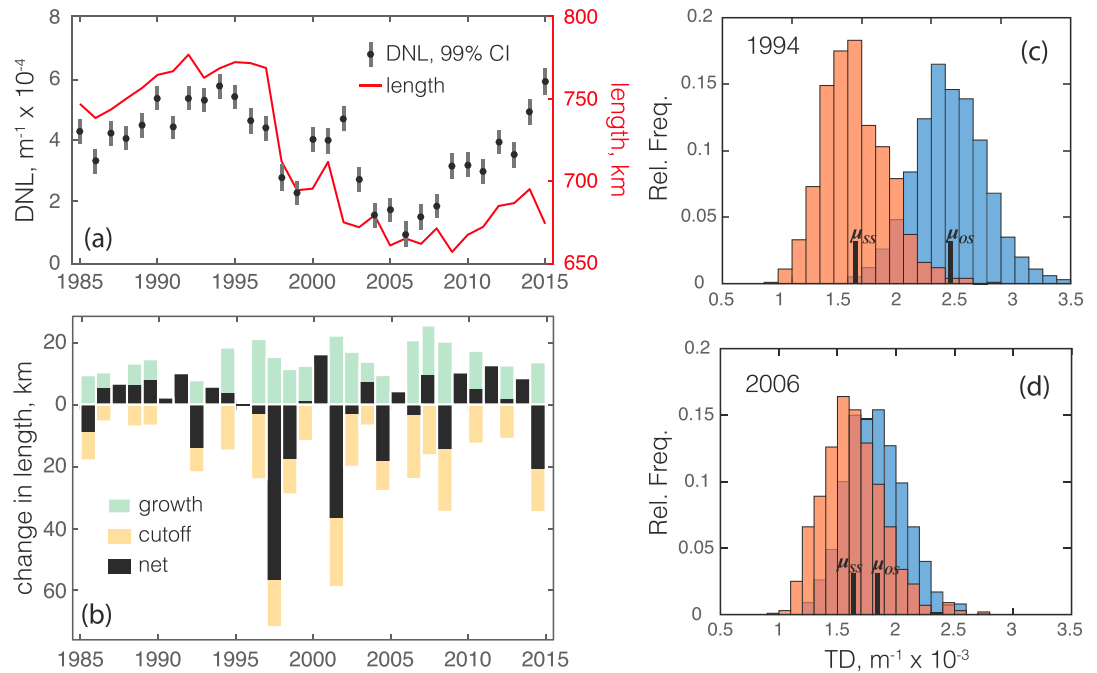


**Figure 6.** (a) Degree of nonlinearity (DNL) is shown by black points with 99% confidence intervals for annual realizations of the actively migrating Ucayali River. The red line shows the evolution of the reach length. (b) The annual balance between reach elongation (green bars) and cutoffs (tan bars) is shown with the net annual change shown by black bars. (c and d) The  $OS_{TD}$  and  $SS_{TD}$  distributions and their means ( $\mu_{OS}$  and  $\mu_{SS}$ ) for the highest (1994) and lowest (2006) DNL over the 30 year period are shown. For both years,  $\mu_{OS}$  and  $\mu_{SS}$  are significantly different, i.e., drawn from different distributions, at the 99% significance level.

the cutoff may also play an important primary role, along with cutoff-induced accelerated planform changes. That is, both the simulation and the Ucayali suggest that a centerline’s degree of nonlinearity is not merely a function of the balance between bend growth and bend removal but may also be modulated by centerline features larger and smaller than the meander bend. In the following section, we investigate this possibility via a multiscale analysis.

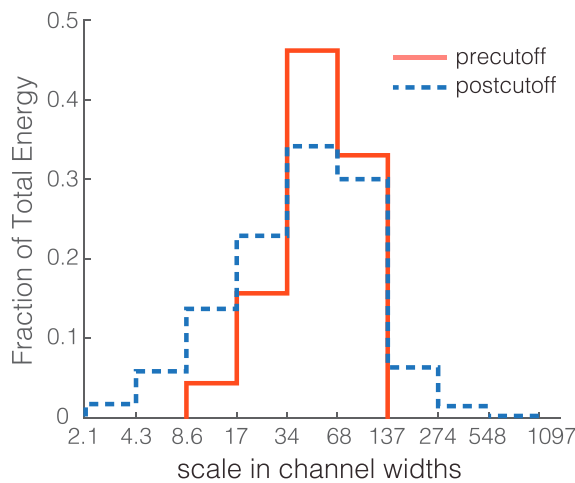


**Figure 7.** A normalized wavelet power spectrum for the precutoff (red) and postcutoff (blue) centerline curvatures is shown. Each distribution represents the summation of wavelet coefficients across all locations normalized by the total energy.

#### 4. The Effect of Cutoffs on Form Nonlinearity

Before the occurrence of cutoffs in our simulation, the source of form nonlinearity measured by the DNL is wholly attributed to the geometric process nonlinearity of equation (1). Before the DNL achieved an approximate steady state, cutoffs’ overall effect was a reduction of the DNL. However, cutoffs themselves are a planform dynamic that might impose form nonlinearity onto the centerline structure. The normalized wavelet power spectrum (Figure 7) demonstrates how cutoffs “spread” the spectral energy of centerline curvatures through the introduction of new scales. Immediately before cutoffs,

the scales corresponding to fully developed individual meander bends (34W–137W for channel width  $W$ ), i.e., those shown by the  $t = 450$  year centerline in Figure 4b, dominated the spectrum. Immediately following cutoffs, the smallest scale features (2.1W–4.3W) were born and grew to fully developed meander bends (34W–137W). Scales larger than the fully developed meander bends (137W–1097W) also developed as meander trains grew in the cross-valley direction. To assess how this cutoff-induced spectral spreading contributed to DNL, a localized space-frequency analysis of the curvatures series was needed to decompose them into a local (e.g., wavelet) rather than a global (e.g., Fourier) basis (section 4.1). This analysis is performed on precutoff and postcutoff centerlines to further unravel the role of cutoffs and bend growth on the degree of nonlinearity (section 4.2).

#### 4.1. Linearizing Surrogates Partially With Gradual Wavelet Reconstruction

Fourier-based linearization provides a way to measure a signal's degree of nonlinearity relative to its fully linearized counterpart, but it does not give insight into which features of the signal (i.e., scales and/or locations) contribute most to its nonlinearity. For that, a localized space-frequency analysis is needed that decomposes the signal into a local (e.g., wavelet) rather than a global (e.g., Fourier) basis. Gradual wavelet reconstruction (GWR) was introduced by Keylock [2010] as a surrogate generation method that allows partial linearization of the original signal.

To perform GWR, a signal was decomposed with a maximal overlap discrete wavelet transform (MODWT) [Percival and Walden, 2006], resulting in  $J \times K$  coefficients  $w_{j,k}$ , where  $J$  is the number of scales of decomposition and  $K$  is the length of the signal. The MODWT is advantageous to use for GWR primarily because it allows the preservation of the power spectrum and autocorrelation function at each scale while providing  $K$  coefficients at each level of decomposition, but see Keylock [2008] for a discussion of its other desirable properties. The total energy  $E$  of the signal is the sum of the squared wavelet coefficients:

$$E = \sum_{j=1}^J \sum_{k=1}^K w_{j,k}^2. \quad (5)$$

A desired fraction of wavelet energy to retain in the surrogate was selected as  $\rho$  ( $0 < \rho < 1$ ). The squared coefficients  $w_{j,k}^2$  were sorted from largest to smallest, and the largest-energy coefficients accounting for  $\rho E$  of the total energy were fixed in place. The IAAFT was applied to each scale of the transform, shuffling the nonfixed wavelet coefficients while preserving the wavelet spectrum. The MODWT was finally inverted to recover a surrogate signal that fixed in place a  $\rho$  fraction of the energy of the original signal. Further details of GWR can be found in Keylock [2007, 2010].

The systematic variation of  $\rho$  allows identification of the wavelet coefficients most important to the nonlinear structure of the signal. Consider generating a surrogate for  $\rho = 1$ . In this trivial case, all the energy of the original signal is fixed in place and the surrogate is therefore no different than the original signal (so the DNL is necessarily zero). Now we proceed to generate surrogates for incrementally reduced values of  $\rho$ ; we used increments of 0.1 herein. Each time  $\rho$  is reduced, additional wavelet coefficients are randomized. Therefore, changes in  $\rho$  correspond to specific coefficients in the wavelet domain which provide scale and/or location information. By measuring the DNL of surrogates generated by incrementally decreasing  $\rho$ , large changes in DNL with respect to  $\rho$  can then be attributed to the specific wavelet coefficients (and hence scales) that were unfixed for that  $\rho$  increment, thus identifying the scales and locations that contribute disproportionately to the signal's nonlinear structure. For  $\rho = 0$ , all coefficients are randomized to create a completely linearized surrogate, and in these cases the Fourier-based surrogate generation method was used.

#### 4.2. Contribution of Cutoffs to DNL

GWR was applied to two curvature signals from the simulated centerline: one immediately before cutoffs began ( $t = 450$  years, Figure 4) and the other once an approximate steady state DNL had been achieved ( $t = 7000$  years). The DNL was measured for both centerlines as  $\rho$  was varied in constant increments of 0.1, or 10% of the total wavelet energy, and the resulting  $\text{DNL}(\rho)$  curves in Figure 8 agree with the results of Figure 4 insofar as the total DNL was higher for centerlines immediately preceding cutoff than those during the postcutoff state. Indeed, total DNL (i.e.,  $\text{DNL}(\rho = 0)$ ) is nearly twice as high for the precutoff centerline.

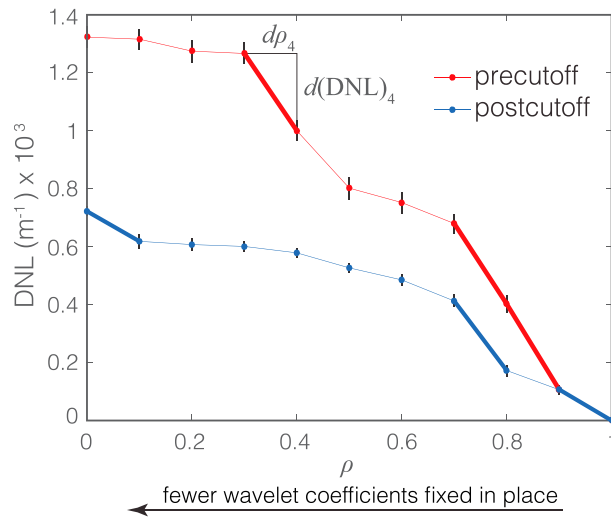


**Figure 8.** The degree of nonlinearity (DNL) is shown as a function of  $\rho$  for precutoff (red) and postcutoff (blue) centerline curvatures, where  $\rho$  is a parameter controlling the amount of nonlinearity preserved in the surrogates. For  $\rho = 1$ , all nonlinearity is preserved, while for  $\rho = 0$ , all nonlinearity is destroyed. With decreasing  $\rho$ , fewer original wavelet coefficients are fixed in place. The trends of these lines indicate that as surrogates become more linear, the difference between the original signal and the surrogates (i.e., DNL) increases. For both the precutoff and postcutoff curvatures, three bold line segments highlight the three largest increments of  $\rho$  that contributed most to the total DNL. The definitions of  $d\rho_i$  and  $d(\text{DNL})_i$  are shown for  $i = 4$ . Total DNL corresponds to  $\rho = 0$ . Confidence intervals at the 99% level are shown at each point by black lines.

bold segments of each centerline accounts for 30% of the total energy, while the DNL contributed by the three bold segments is  $\sum_{i=4,8,9} d(\text{DNL})_i / \sum_{i=1}^N d(\text{DNL})_i = 63.4\%$  of the total DNL for the precutoff and  $\sum_{i=1,8,10} d(\text{DNL})_i / \sum_{i=1}^N d(\text{DNL})_i = 62.3\%$  for the postcutoff centerlines. The coefficients from the three largest contributing increments to DNL were summed across all locations in the wavelet transform to identify those scales of the original signal that were most important to the overall nonlinearity. In Figure 9, these scales are shown on top of the wavelet power spectrums of the original signals. The postcutoff spectrum indicates that the scales created by cutoff activity ( $<8.6^\circ\text{W}$  and  $>137^\circ\text{W}$ ) are significant contributors to the total

Confidence intervals for each value of  $\rho$  indicate that significant difference between precutoff and postcutoff centerlines emerges at  $\rho = 0.8$ .

The slopes of the  $\text{DNL}(\rho)$  curves in Figure 8 indicate which  $\rho$  increments and, therefore, which wavelet coefficients are most important in accounting for total DNL. These slopes can be written as  $d(\text{DNL})_i / d\rho_i$  for the  $i$ th increment of  $\rho$ , where  $d\rho_i = 0.1$  for all  $i$ . In other words, for each incremental reduction of  $\rho$ , 10% less of the total wavelet energy from the original signal is fixed in place in the surrogates. The three steepest slopes (shown by bold line segments) correspond to the three largest  $d(\text{DNL})_i$  increments, i.e., those that contributed the most to the total DNL. Recall that total DNL is measured against surrogates that have  $\rho = 0$ . Total DNL may also be written as the sum of the contributing increments: total  $\text{DNL} = \text{DNL}(\rho = 0) = \sum_{i=1}^N d(\text{DNL})_i$  for  $N = 10$  increments. The wavelet energy accounted for by the three

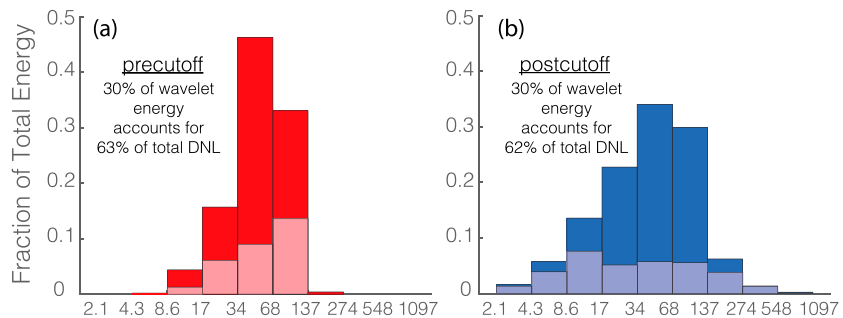


**Figure 9.** The normalized wavelet power spectra are shown for (a) precutoff (dark bars) and (b) postcutoff (dark bars) centerlines, as in Figure 7. The lighter bars in Figures 9a and 9b represent the most energetic 30% of the total wavelet energy and account for 63% (precutoff) and 62% (postcutoff) of the total DNL. Total DNL is much higher in precutoff ( $1.3 \text{ km}^{-1}$ ) than postcutoff ( $0.72 \text{ km}^{-1}$ ) centerlines. The lighter bars represent the scales that contribute disproportionately more to the total DNL and correspond to the summation of the scales of the bold line segments in Figure 8. The lighter colors represent 30% of the total energy of the original centerline signals but account for 63% and 62% of the total DNL in the precutoff and postcutoff centerlines, respectively.

DNL. The energy contained at scales representing fully developed meander bends ( $>17^\circ\text{W}$  and  $<137^\circ\text{W}$ ) decreased from 95% of the total energy for the precutoff centerline to 87% of the postcutoff total energy. That is, only 8% of the total energy was lost from the meander bend scale after cutoffs began. Yet the relative contributions of these scales to the DNL decreased from 95% (precutoff) to 54% (postcutoff). In other words, although developed meander bends scales were still abundant after cutoffs occurred, their contributions to the DNL were significantly diminished.

## 5. Discussion

Significant form nonlinearity was identified in all the of centerline curvature series we analyzed, including three natural rivers and one simulated. Previous attempts to quantify form nonlinearity from meandering river centerlines found no compelling evidence for its presence [Perucca *et al.*, 2005; Frascati and Lanzoni, 2013]. These studies similarly cast centerline curvature series into phase space and performed various tests of nonlinearity on the reconstructed trajectories. The transportation distance (TD) we employed measured significant difference between the trajectory densities of each original signal and their corresponding linear surrogates, indicating that a nonlinear system generated the original signals' trajectory geometries. The discovery of form nonlinearities presented in this paper (Figures 3 and 4) establishes for the first time that process nonlinearities are indeed encoded in the meander planform structure. Identified form nonlinearities also lend credence to conceptual models of meandering river morphodynamics, including chaos [Montgomery, 1993; Frascati and Lanzoni, 2010] and self-organized criticality [Stolum, 1996, 1998; Fonstad and Marcus, 2003] that arise from nonlinear dynamical systems.

### 5.1. Process Nonlinearity Expressed Through Form Nonlinearity in Meandering Rivers

Measuring the evolution of the DNL in natural rivers and synthetically generated centerlines provides insight into how nonlinear processes contribute to form nonlinearity. Only two sources of process nonlinearity acted on the simulated centerline, which evolved under linearized and decoupled treatments of hydrodynamics and sediment dynamics. The first is the geometric process nonlinearity evident from equation (1), and the second is the action of cutoffs. Before cutoffs began, the DNL grew monotonically as bends became enlarged and skewed. As the precutoff centerline evolved, the expression of the process nonlinearity through the form nonlinearity became stronger, suggesting that the inference of process nonlinearity from form nonlinearity depends somewhat on the duration over which the process nonlinearities act. Only after cutoffs began did the DNL decrease due to the sudden removal of the fully developed bends that had sufficient time to express the underlying geometric process nonlinearity in their morphologies. Cutoffs therefore weakened the expression of process nonlinearity through planform structure. However, even after the inception of cutoffs the DNL continued to increase until a balance was eventually achieved between the expression of process nonlinearity and the action of cutoffs to erase its manifestation in the planform.

Previously, cutoffs had been argued to reduce the overall nonlinearity in meandering river spatial structure through the removal of bends that had sufficient time to express inherent deterministic (process) nonlinearities [Perucca *et al.*, 2005; Camporeale *et al.*, 2008]. Our analysis with gradual wavelet reconstruction (GWR) suggests a more subtle reasoning; the degree to which cutoffs destroy planform nonlinearity depends also on the position of the removed bend(s) relative to its neighbors in a meander train. The power spectra of precutoff and postcutoff centerlines showed that cutoffs spread the spectral energy of the curvature signal into a wider range of scales. However, cutoffs reduced the energy contained by scales representing fully developed bends by only 8% of the total spectral energy, yet the relative contributions of these scales to the total DNL decreased by 41%. In other words, although the emergent bend scales were still present in the meander train after cutoffs were active, they were significantly less effective in expressing form nonlinearity. This discrepancy is attributable to cutoffs breaking the nonlinear patterns of bend arrangement within a meander train that is expressed through an altered topological structure in the embedding space. The transportation distance, and therefore the DNL, measures differences between trajectories that are reconstructed via lagged vectors of the input signals (equation (2)). A cutoff can therefore remove a portion of the curvature signal such that trajectories that were locally dense in the phase space before cutoff become dispersed due to a discontinuous shift in the lagged vectors. This hypothesis that the effect of a cutoff on form nonlinearity depends on its location is supported by the evolution of DNL for simulated centerlines, where initially meander trains were somewhat synchronized but became more fragmented as the

simulation progressed (Figure 4b). Despite the occurrence of cutoffs, the DNL remained above its long-term average for approximately 1500 years.

### 5.2. What Does DNL Measure?

Two Minnesota rivers, the Ucayali River in Peru, and analysis of the simulated river suggest that bend growth promotes DNL, while cutoffs generally act to reduce DNL despite the additional nonlinearity imposed by cutoffs. However, the reduction in length due to cutoff did not simply relate to a corresponding decrease in DNL. Predicting how an individual cutoff event affects overall form nonlinearity is not straightforward. The difficulty in determining the degree to which a particular cutoff will affect the DNL can be attributed to both the dependence of DNL on the location of the cutoff within the meander train and the simultaneous evolution of the rest of the centerline. Following a major, triple-bend cutoff, the Ucayali River showed that the planform evolution of the entire meander train responded rapidly enough to return to precutoff DNL levels although the river's length (or sinuosity) remained substantially lower than before the cutoff. The magnitudes of and changes in DNL were not significantly correlated with cutoff lengths, elongation lengths, or net change in length. These results are not entirely unexpected, as the DNL measures nonlinear structure within the phase space making the interpretation of DNL in terms of physical system characteristics nontrivial. Interpretation of DNL requires developing a refined understanding of how centerline evolutions and cutoffs are manifest within the phase space constructed via delay embedding made possible through Takens' theorem [Takens, 1981].

Although our analysis does not provide how individual cutoffs or bend growths and deformations affect form nonlinearity, it does suggest that the steady state DNL characterizes the local processes driving a meandering river's evolution. The steady state DNL should thus distinguish between simulations that incorporate process nonlinearities associated with hydrodynamics or sediment dynamics from those with linearized dynamics.

### 5.3. Scale Dependence and (Non)normalization of the DNL

The magnitude of DNL is a function of the scale of the TD distributions, and TD is a function of the scale of the input data. The DNL is therefore generally not comparable between various systems without carefully selected normalizations. In our case, the DNL contains some scale dependence due to the dependence of the curvature signal statistics on centerline sampling density and smoothing techniques [Crosato, 2007; Güneralp and Rhoads, 2007]. The problem of scale dependence of sampling and smoothing of centerlines on curvature signals is beyond the scope of this work and requires further investigation, especially considering the widespread use of curvature signals to characterize aspects of meandering river planforms. However, a consistent basis for obtaining comparable curvatures derived from different data sources and rivers of various scales is a prerequisite for comparing DNL between rivers. We chose not to normalize DNL measures by a characteristic reach scale (e.g., channel width or dominant wavelength) for two reasons. First, because meander train planforms are multiscale features, selecting a single characteristic value may bias the normalized DNL, although promising recent research has grappled with the multiscale structure of meandering rivers using wavelets [Gutierrez and Abad, 2014; Vermeulen et al., 2016; Zolezzi and Güneralp, 2015]. Second, the classic normalization constants may not actually be constant nor stationary. Average width for both the Ucayali and Blue Earth Rivers increased nearly 20% over the relatively short periods of our analysis. The spatial variations in width along the centerline may also be significant. For example, the Ucayali's channel width varied from 400 to over 1300 m along its course [Schwenk et al., 2016, Figure 14].

Normalization may also be performed using variables specific to the analysis itself. For example, the DNL could be normalized by properties of the  $OS_{TD}$  and/or  $SS_{TD}$  distributions. However, the statistics of these distributions nontrivially depend on the original signal structure and the parameterizations of the surrogate generation and embedding techniques. Without a full understanding of this dependence, we found normalization with such variables to obscure rather than clarify interpretation of our results. The decision not to normalize means that degrees of nonlinearity measured by the DNL for different rivers are not directly comparable. Ultimately, however, the observed presence (or absence) of nonlinearity is unaffected by normalization, and changes in DNL in time for the same river are also comparable since biases due to sampling and smoothing techniques are consistent.

## 6. Conclusions and Future Directions

In this work we developed a framework for identifying form nonlinearities from the centerline configuration of meandering rivers. We relied on Takens' theorem to reconstruct trajectories of the dynamical systems governing meandering river evolution under the assumption that the spatial structure of the centerline acts as a sufficient measurement on the system dynamics. To assess whether known process nonlinearities (due to hydrodynamics, sediment dynamics, cutoffs, and migration dynamics) are indeed manifest as form nonlinearities (those contained in centerline morphologies), curvature series were compared against linearized versions of themselves in phase space. Significant difference between the two implied nonlinearity of the underlying meandering dynamics and the magnitude of their difference was measured by the degree of nonlinearity (DNL). Investigation of the effects of meander growth and cutoffs on form nonlinearity via the DNL found that

1. Form nonlinearities were clearly identified in three natural rivers and one simulated meandering centerline, partially validating the assumption that meandering river centerline geometries encode process nonlinearities.
2. In agreement with previous findings, process nonlinearities acting to grow and deform bends contribute to form nonlinearity, while cutoffs tend to erode form nonlinearity.
3. Cutoffs also act as sources of form nonlinearity themselves by creating high-frequency scales within centerlines and interacting with local process nonlinearities to allow low-frequency centerline wandering. These new scales contributed disproportionately to DNL.
4. The magnitude of form nonlinearity measured by the DNL is not simply related to centerline growths and cutoffs but also depends on the spatial arrangement of bends and location of growth or cutoff within a meander train, highlighting the importance of understanding the whole-system dynamics in addition to individual bends

Our model featured linearized flow and sediment dynamics and a linear bank erosion law. While this model was appropriate for isolating the effects of cutoffs and the inherent geometric process nonlinearities of meander evolution, detailed nonlinear process models should be implemented to quantify the effects of local, nonlinear hydrodynamics, and sediment dynamics. Such modeling efforts could determine if different process nonlinearities leave unique signatures on the planform spatial structure, and the steady state DNL could then potentially isolate and identify nonlinear processes from observations of planform morphology alone. We detected nonlinear structure from trajectory densities in phase space, confirming that process nonlinearity in the underlying deterministic dynamics of meandering river evolution indeed leaves its signature on the resulting planform, but we made no attempt to model the trajectories themselves. Our establishment of form nonlinearities in meandering river centerlines calls for renewed attempts to exploit this nonlinear structure by further analysis of trajectory structure within the phase space and development of phase space models. Finally, deeper physical intuition of the DNL should be developed through numerical experimentation to establish it as a metric that connects both form and process.

## Appendix A: Obtaining the Centerline Curvature Signal

The spatial series of centerline curvatures used here to characterize meandering river planform morphology is given by

$$C(s) = d\theta(s)/ds \quad (A1)$$

where  $C$  is the curvature,  $s$  is the along-stream distance, and  $\theta$  is the channel direction defined discretely as  $\theta_i = \tan^{-1}(y_{i+1} - y_i / x_{i+1} - x_i)$  for any two adjacent  $x, y$  centerline nodes. As the derivative of the channel angle, the curvature removes linear trends imposed by nonstationarities due to valley forcing or large-scale heterogeneity in floodplain resistance, vegetation, etc. while capturing bend planform structure.

Meandering river centerlines may either be digitized directly by hand from aerial imagery or maps [Hooke, 1977] or calculated somewhat indirectly from digitization of banklines which may also be obtained by hand [Bevis, 2015] or through image processing. The choice of technique ultimately determines the sampling resolution and error. For measurements made directly on the centerline, such as meander wavelength and

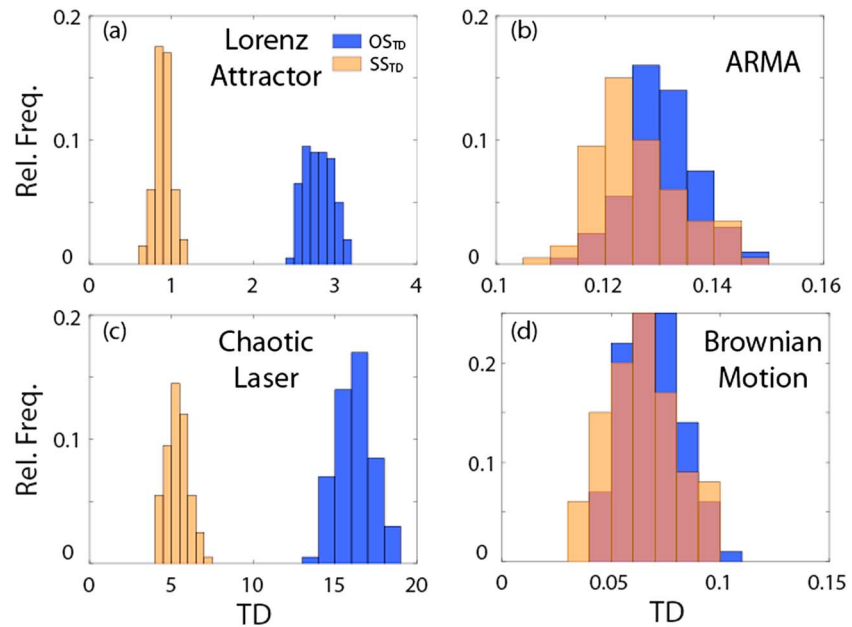


**Figure B1.** Distributions are shown for surrogate surrogate ( $SS_{TD}$ , in orange) TDs and original surrogate ( $OS_{TD}$ , in blue) TDs for four series: (a) the Lorenz “butterfly” attractor, (b) a linear ARMA(1,1) series [Granger *et al.*, 1978], (c) time series from a chaotic laser provided as part of the Santa Fe Institute competition series, and (d) a linear random-walk process. The degree of nonlinearity (DNL) is measured as the difference between the means of the  $OS_{TD}$  and  $SS_{TD}$  distributions.

amplitude, errors associated with the digitization process are usually negligible. However, because curvature is a derivative measurement, errors in the original centerline discretization are magnified in the curvature signal and smoothing is required. The techniques presented here for acquiring curvature series with fidelity to the observed centerlines were developed using both hand-delineated (Minnesota rivers) and image processed centerlines (Ucayali River).

After the centerlines were digitized, their  $x$  and  $y$  coordinates were smoothed with a Savitzky-Golay filter. A “temporary” curvature signal was computed according to equation (A1), and the number of bends  $N_b$  in the reach was estimated as the number of times this curvature signal crossed zero. A bend therefore was defined as a reach of river between two inflection points. The number of bends was verified by eye and was noted to vary depending on the strength of the Savitzky-Golay smoothing filter due to the multiscale nature of meandering planforms [Gutierrez and Abad, 2014]. The smoothed centerline was then resampled with evenly spaced nodes with a density of  $25N_b$  such that each bend contained 25 nodes on average. New nodes were interpolated by fitting piecewise parametric cubic splines to the smooth centerline [Güneralp and Rhoads, 2007] and integrating along the splines every  $L / 25N_b$ , where  $L$  is the length of the reach. Finally, the curvature series was computed on the smoothed, evenly spaced centerline according to equation (A1).

### Appendix B: Computing the Transportation Distance

Given two series in an embedding space (in our case an original signal and its surrogate), the transportation distance (TD) metric [Moekel and Murray, 1997] was used to compute their difference. Two series  $F$  and  $G$  were embedded within a phase space according to equation (2). The domain occupied by  $F$  and  $G$  was discretized into  $B$  boxes by dividing each  $m_i$  axis into  $B^{1/m}$  intervals. The probability that series  $F$  occupies any box  $B_i$  was estimated as  $f_i(B_i) = N(F, B_i) / N(F)$ , where  $N(F, B_i)$  is the number of points in series  $F$  that lie within box  $B_i$  and  $N(F)$  is the length of series  $F$ . The discretization of each  $m_i$  axis intervals may be performed such that either (a) each interval is the same size (equally spaced bins) or (b) each interval contains the same probability (equal probability bins). We employed the latter method herein as it added robustness against outliers.

Now let  $\mu_{ij} > 0$  represent the amount of probability transported from box  $B_i$  to  $B_j$  according to transportation plan  $\mu$ . To preserve initial and final distributions of  $F$  and  $G$ , the following conditions must be met:  $\sum_{j=1}^N \mu_{ij} = f_i$  and  $\sum_{i=1}^N \mu_{ij} = g_j$ . Finally, let  $M(f, g)$  represent all transportation plans meeting these requirements, and then the transportation distance (TD) may be defined as the minimized transportation cost:

$$\text{TD}(g, h) = \inf_{\mu \in M(g, h)} \sum_{i, j=1}^N \mu_{ij} \delta_{ij} \quad (\text{B1})$$

where  $\delta_{ij}$  is a distance metric normalized to the embedding dimension between the centers of  $B_i$  and  $B_j$ . Thus, the TD effectively measures the least amount of work required to ensure equal probability of both series  $F$  and  $B$  in all  $B_i$  boxes. We also note that since the axes of the embedding space have the units of the input data, the distance traveled by shipped probabilities and therefore the TD are computed in units of the input data. The number of intervals used to discretize each axis of the phase space was chosen according to the following formula:

$$B^{1/m} = \min\left(8, \text{floor}\left(\left(N/5\right)^{1/m} - 1\right)\right) \quad (\text{B2})$$

The ability of the TD to discriminate between some common linear and nonlinear signals is shown in Figure B1, and a more detailed development of TD is given by *Moeckel and Murray [1997]*.

#### Acknowledgments

This research was funded by NSF grant EAR-1209402 under the Water Sustainability and Climate Program (WSC): REACH (REsilience under Accelerated CHange) and benefited from collaborations made possible by NSF grant EAR-1242458 under Science Across Virtual Institutes (SAVI): LIFE (Linked Institutions for Future Earth). J.P.S. acknowledges support provided by an NSF Graduate Research Fellowship. We thank Chris Keylock for providing GWR and TD algorithms which may be downloaded from <https://water.shef.ac.uk/software/>, Martin Bevis at the University of Minnesota-Duluth for providing hand-delineated banklines for the two Minnesota rivers, and Ankush Khandelwal, Eric McCaleb, Mace Blank, and Anuj Karpatne of the University of Minnesota's Computer Science Department for helping obtain, classify, and composite Landsat imagery of the Ucayali River. Mulu Fratkin at the University of Minnesota assisted with Landsat image quality control and processing. Landsat imagery was downloaded from the Google Earth Engine API, and channel traces of the Blue Earth and Watonwan Rivers may be downloaded as supporting information from *Bevis [2015]* at <https://doi.org/10.13020/D6XS3V>. Finally, this work benefitted from conversations with Stefano Lanzoni at the University of Padova and William Dietrich at the University of California, Berkeley, as well as insightful comments and questions from an anonymous reviewer, the Associate Editor, and Editor John Buffington.

#### References

- Abarbanel, D. I., and M. B. Kennel (1993), Local false nearest neighbors and dynamical dimensions from observed chaotic data, *Phys. Rev. E*, *47*(5), 3057–3068, doi:10.1103/PhysRevE.47.3057.
- Bak, P., C. Tang, and K. Wiesenfeld (1987), Self-organized criticality: An explanation of the 1/f noise, *Phys. Rev. Lett.*, *59*(4), 381–384, doi:10.1103/PhysRevLett.59.381.
- Basu, S., and E. Foufoula-Georgiou (2002), Detection of nonlinearity and chaoticity in time series using the transportation distance function, *Phys. Lett. A*, *301*(5–6), 413–423, doi:10.1016/S0375-9601(02)01083-6.
- Bevis, M. (2015), *Sediment Budgets Indicate Pleistocene Base Level Fall Drives Erosion in Minnesota's Greater Blue Earth River Basin*, pp. 1–96, Univ. of Minnesota, Duluth, Minn.
- Blanckaert, K., and H. J. de Vriend (2010), Meander dynamics: A nonlinear model without curvature restrictions for flow in open-channel bends, *J. Geophys. Res.*, *115*, F04011, doi:10.1029/2009JF001301.
- Blanckaert, K., G. Constantinescu, W. Uijttewaald, and Q. Chen (2013), Hydro- and morphodynamics in curved river reaches—Recent results and directions for future research, *Adv. Geosci.*, *37*, 19–25, doi:10.5194/adgeo-37-19-2013.
- Callander, R. A. (1969), Instability and river channels, *J. Fluid Mech.*, *36*(3), 465–480, doi:10.1017/S0022112069001765.
- Camporeale, C., P. Perona, A. Porporato, and L. Ridolfi (2007), Hierarchy of models for meandering rivers and related morphodynamic processes, *Rev. Geophys.*, *45*, RG1001, doi:10.1029/2005RG000185.
- Camporeale, C., E. Perucca, and L. Ridolfi (2008), Significance of cutoff in meandering river dynamics, *J. Geophys. Res.*, *113*, F01001, doi:10.1029/2006JF000694.
- Constantinescu, G., S. Miyawaki, B. L. Rhoads, and A. Sukhodolov (2014), Numerical evaluation of the effects of planform geometry and inflow conditions on flow, turbulence structure, and bed shear velocity at a stream confluence with a concordant bed, *J. Geophys. Res. Earth Surf.*, *119*, 2079–2097, doi:10.1002/2014JF003244.
- Crosato, A. (2007), Effects of smoothing and regridding in numerical meander migration models, *Water Resour. Res.*, *43*, W01401, doi:10.1029/2006WR005087.
- Fonstad, M., and W. A. Marcus (2003), Self-organized criticality in riverbank systems, *Ann. Assoc. Am. Geogr.*, *93*(2), 281–296, doi:10.1111/1467-8306.9302002.
- Foufoula-Georgiou, E., Z. Takbiri, J. A. Czuba, and J. Schwenk (2015), The change of nature and the nature of change in agricultural landscapes: Hydrologic regime shifts modulate ecological transitions, *Water Resour. Res.*, *51*, 6649–6671, doi:10.1002/2015WR017637.
- Frascati, A., and S. Lanzoni (2010), Long-term river meandering as a part of chaotic dynamics? A contribution from mathematical modelling, *Earth Surf. Processes Landforms*, *35*, 791–802, doi:10.1002/esp.1974.
- Frascati, A., and S. Lanzoni (2013), A mathematical model for meandering rivers with varying width, *J. Geophys. Res. Earth Surf.*, *118*, 1641–1657, doi:10.1002/jgrf.20084.
- Granger, C., J. William, and A. P. Andersen (1978), *An Introduction to Bilinear Time Series Models*, Vandenhoeck & Ruprecht.
- Güneralp, I., and R. A. Marston (2012), Process-form linkages in meander morphodynamics: Bridging theoretical modeling and real world complexity, *Prog. Phys. Geogr.*, *36*(6), 718–746, doi:10.1177/0309133312451989.
- Güneralp, I., and B. L. Rhoads (2007), Continuous characterization of the planform geometry and curvature of meandering rivers, *Geogr. Anal.*, *40*(1), 1–25, doi:10.1111/j.0016-7363.2007.00711.x.
- Gutierrez, R. R., and J. D. Abad (2014), On the analysis of the medium term planform dynamics of meandering rivers, *Water Resour. Res.*, *50*, 3714–3733, doi:10.1002/2012WR013358.
- Hegger, R., H. Kantz, and T. Schreiber (1999), Practical implementation of nonlinear time series methods: The TISEAN package, *Chaos*, *9*(2), 413–435, doi:10.1063/1.166424.

- Hooke, J. M. (1977), The distribution and nature of changes in river channel patterns: The example of Devon, in *River Channel Changes*, edited by K. J. Gregory, pp. 265–280, Wiley, New York.
- Hooke, J. M. (2004), Cutoffs galore!: Occurrence and causes of multiple cutoffs on a meandering river, *Geomorphology*, *61*, 225–238, doi:10.1016/j.geomorph.2003.12.006.
- Ikeda, S., G. Parker, and K. Sawai (1981), Bend theory of river meanders. Part 1. Linear development, *J. Fluid Mech.*, *112*, 363–377, doi:10.1017/S0022112081000451.
- Imran, J., G. Parker, and C. Pirmez (1999), A nonlinear model of flow in meandering submarine and subaerial channels, *J. Fluid Mech.*, *400*, 295–331, doi:10.1017/S0022112099006515.
- Johannesson, H., and G. Parker (1989), Velocity redistribution in meandering rivers, *J. Hydraul. Eng.*, *115*(8), 1019–1039, doi:10.1061/(ASCE)0733-9429(1989)115:8(1019).
- Kang, S., and F. Sotiropoulos (2012), Assessing the predictive capabilities of isotropic, eddy viscosity Reynolds-averaged turbulence models in a natural-like meandering channel, *Water Resour. Res.*, *48*, W06505, doi:10.1029/2011WR011375.
- Kantorovich, L. V. (1942), On the transfer of masses, *Dokl. Akad. Nauk SSSR*, *37*(7–8).
- Kantz, H., and T. Schreiber (2004), *Nonlinear Time Series Analysis*, Cambridge Univ. Press.
- Keylock, C. J. (2007), A wavelet-based method for surrogate data generation, *Physica D*, *225*(2), 219–228, doi:10.1016/j.physd.2006.10.012.
- Keylock, C. J. (2008), Improved preservation of autocorrelative structure in surrogate data using an initial wavelet step, *Nonlinear Processes Geophys.*, *435–444*, doi:10.5194/npg-15-435-2008.
- Keylock, C. J. (2010), Characterizing the structure of nonlinear systems using gradual wavelet reconstruction, *Nonlinear Processes Geophys.*, *17*(6), 615–632, doi:10.5194/npg-17-615-2010.
- Keylock, C. J., G. Constantinescu, and R. J. Hardy (2012), The application of computational fluid dynamics to natural river channels: Eddy resolving versus mean flow approaches, *Geomorphology*, *179*, 1–20, doi:10.1016/j.geomorph.2012.09.006.
- Keylock, C. J., A. Singh, and E. Foufoula-Georgiou (2014), The complexity of gravel bed river topography examined with gradual wavelet reconstruction, *J. Geophys. Res. Earth Surf.*, *119*, 682–700, doi:10.1002/2013JF002999.
- Lane, S. N., and K. Richards (1997), Linking river channel form and process: Time, space and causality revisited, *Earth Surf. Processes Landforms*, *22*, 249–260, doi:10.1002/(SICI)1096-9837(199703)22:3<249::AID-ESP752>3.0.CO;2-7.
- Legleiter, C. J. (2014), A geostatistical framework for quantifying the reach-scale spatial structure of river morphology: 1. Variogram models, related metrics, and relation to channel form, *Geomorphology*, *205*, 65–84, doi:10.1016/j.geomorph.2012.01.016.
- Moeckel, R., and B. Murray (1997), Measuring the distance between time series, *Physica D*, *102*, 187–194, doi:10.1016/S0167-2789(96)00154-6.
- Montgomery, K. (1993), Non-linear dynamics and river meandering, *Area*, *25*(2), 97–108, doi:10.2307/20003236.
- Motta, D., J. D. Abad, E. J. Langendoen, and M. H. Garcia (2012), A simplified 2D model for meander migration with physically-based bank evolution, *Geomorphology*, *163–164*, 10–25, doi:10.1016/j.geomorph.2011.06.036.
- Ning, L., T. T. Georgiou, and A. Tannenbaum (2015), On matrix-valued Monge-Kantorovich optimal mass transport, *IEEE Trans. Autom. Control*, *60*(2), 373–382, doi:10.1109/TAC.2014.2350171.
- Parker, G., K. Sawai, and S. Ikeda (1982), Bend theory of river meanders. Part 2. Nonlinear deformation of finite-amplitude bends, *J. Fluid Mech.*, *115*, 303–314, doi:10.1017/S0022112082000767.
- Percival, D. B., and A. T. Walden (2006), *Wavelet Methods for Time Series Analysis*, Cambridge Univ. Press, New York.
- Perucca, E., C. Camporeale, and L. Ridolfi (2005), Nonlinear analysis of the geometry of meandering rivers, *Geophys. Res. Lett.*, *32*, L03402, doi:10.1029/2004GL021966.
- Pittaluga, M. B., and G. Seminara (2011), Nonlinearity and unsteadiness in river meandering: A review of progress in theory and modelling, *Earth Surf. Processes Landforms*, *36*(1), 20–38, doi:10.1002/esp.2089.
- Rubner, Y., C. Tomasi, and L. J. Guibas (2000), The Earth mover's distance as a metric for image retrieval, *Int. J. Comput. Vis.*, *40*(2), 99–121, doi:10.1023/A:1026543900054.
- Rüther, N., and N. R. B. Olsen (2007), Modelling free-forming meander evolution in a laboratory channel using three-dimensional computational fluid dynamics, *Geomorphology*, *89*(3–4), 308–319, doi:10.1016/j.geomorph.2006.12.009.
- Schreiber, T., and A. Schmitz (1996), Improved surrogate data for nonlinearity tests, *Phys. Rev. Lett.*, *635*, 1–4, doi:10.1103/PhysRevLett.77.635.
- Schreiber, T., and A. Schmitz (2000), Surrogate time series, *Physica D*, *142*(3–4), 346–382, doi:10.1016/S0167-2789(00)00043-9.
- Schwenk, J., and E. Foufoula-Georgiou (2016), Meander cutoffs nonlocally accelerate upstream and downstream migration and channel widening, *Geophys. Res. Lett.*, *43*(24), 12,437–12,445, doi:10.1002/2016GL071670.
- Schwenk, J., S. Lanzoni, and E. Foufoula-Georgiou (2015), The life of a meander bend: Connecting shape and dynamics via analysis of a numerical model, *J. Geophys. Res. Earth Surf.*, *120*, 690–710, doi:10.1002/2014JF003252.
- Schwenk, J., A. Khandelwal, M. Fratkin, V. Kumar, and E. Foufoula-Georgiou (2016), High spatio-temporal resolution of river planform dynamics from Landsat: The RivMAP toolbox and results from the Ucayali River, *Earth Space Sci.*, doi:10.1002/2016EA000196.
- Seminara, G. (2006), Meanders, *J. Fluid Mech.*, *554*, 271–297, doi:10.1017/S0022112006008925.
- Seminara, G., G. Zolezzi, M. Tubino, and D. Zardi (2001), Downstream and upstream influence in river meandering. Part 2. Planimetric development, *J. Fluid Mech.*, *438*, doi:10.1017/S0022112001004281.
- Smith, J. D., and S. R. McLean (1984), A model for flow in meandering streams, *Water Resour. Res.*, *20*(9), 1301–1315, doi:10.1029/WR020i009p01301.
- Stolum, H.-H. (1996), River meandering as a self-organization process, *Science*, *271*(5256), 1710–1713, doi:10.1126/science.271.5256.1710.
- Stolum, H.-H. (1997), Fluctuations at the self-organized critical state, *Phys. Rev. E*, *56*(6), 6710–6718, doi:10.1103/physreve.56.6710.
- Stolum, H.-H. (1998), Planform geometry and dynamics of meandering rivers, *Geol. Soc. Am. Bull.*, *110*(11), 1485–1498, doi:10.1130/0016-7606(1998)110<1485:PGADOM>2.3.CO;2.
- Struikma, N., K. W. Olesen, C. Flokstra, and H. J. De Vriend (1985), Bed deformation in curved alluvial channels, *J. Hydraul. Res.*, *23*(1), 57–79, doi:10.1080/00221688509499377.
- Sun, T., P. Meakin, and T. Jøssang (2001), A computer model for meandering rivers with multiple bed load sediment sizes: 1. Theory, *Water Resour. Res.*, *37*(8), 2227–2241, doi:10.1029/2000WR900396.
- Takens, F. (1981), Detecting strange attractors in turbulence, in *Dynamical Systems and Turbulence, Warwick 1980*, vol. 898, pp. 366–381, Springer, Berlin, Heidelberg.
- Theiler, J., S. Eubank, A. Longtin, and B. Galdrikian (1992), Testing for nonlinearity in time series: The method of surrogate data, *Physica D*, *58*, 77–94, doi:10.1016/0167-2789(92)90102-S.

- Venema, V., F. Ament, and C. Simmer (2006), A stochastic iterative amplitude adjusted Fourier transform algorithm with improved accuracy, *Nonlinear Processes Geophys.*, *13*(3), 321–328, doi:10.5194/npg-13-321-2006.
- Vermeulen, B., A. J. F. Hoitink, G. Zolezzi, J. D. Abad, and R. Aalto (2016), Multi-scale structure of meanders, *Geophys. Res. Lett.*, *43*, 3288–3297, doi:10.1002/2016GL068238.
- Zolezzi, G., and I. Güneralp (2015), Continuous wavelet characterization of the wavelengths and regularity of meandering rivers, *Geomorphology*, *252*, 98–111, doi:10.1016/j.geomorph.2015.07.029.